CrossMark

Green synthesis of earth-abundant metal sulfides (FeS$_2$, CuS, and NiS$_2$) and their use as visible-light active photocatalysts for H$_2$ generation and dye removal

Ali M. Huerta-Flores[1,2] · Leticia M. Torres-Martínez[2] · Edgar Moctezuma[1] · Aadesh P. Singh[3] · Björn Wickman[3]

Abstract

Earth-abundant metal sulfides (for example, FeS$_2$, CuS, and NiS$_2$) are promising materials to be used as photocatalysts due to their suitable electronic and optical properties. In this work, we present a fast and low-cost hydrothermal method to synthesize these materials. They are integrally characterized and evaluated as photocatalysts for the H$_2$ evolution reaction and the degradation of indigo carmine (IC). FeS$_2$ exhibits the highest photocatalytic efficiency (32 μmol g^{-1} h^{-1} of H$_2$ evolution and 88% of indigo carmine degradation) under visible light, and this activity is attributed to a larger crystallite size, smaller particle size, and lower recombination, compared to CuS and NiS$_2$. Moreover, three different sacrificial reagents are studied for the H$_2$ evolution reaction, including Na$_2$S/Na$_2$SO$_3$, EDTA, and ethanol. Na$_2$S/Na$_2$SO$_3$ shows the highest enhancement in the activity, increasing the rate of H$_2$ production more than 15 times. This behavior is related to the lower oxidation potential of Na$_2$S/Na$_2$SO$_3$. Moreover, we evaluate the activity of the materials for the electrochemical hydrogen evolution reaction (HER). In summary, this work provides valuable information for effective applications of these earth-abundant metal sulfides for energy and environmental photocatalytic processes.

1 Introduction

The development of earth-abundant visible light active materials is of prime importance for their technological use in energy and environmental processes. The main applications include photocatalytic hydrogen evolution, carbon dioxide reduction and the degradation of organic compounds in water [1, 2]. Metal sulfides have attracted considerable

✉ Leticia M. Torres-Martínez
lettorresg@yahoo.com

1 Facultad de Ciencias Químicas, Universidad Autónoma de San Luis Potosí, Av. Manuel Nava #6, 78290 San Luis Potosí, S.L.P., Mexico

2 Departamento de Ecomateriales y Energía, Facultad de Ingeniería Civil, Universidad Autónoma de Nuevo León, UANL, Av. Universidad S/N Ciudad Universitaria, C.P. 66455 San Nicolás de los Garza, Nuevo León, Mexico

3 Division of Chemical Physics, Department of Physics, Chalmers University of Technology, 412 96 Gothenburg, Sweden

interest due to their promising properties for electronic and optical applications [3]. FeS$_2$, CuS, and NiS$_2$ are abundant and non-toxic materials with small band gaps (1.3–1.8 eV) and high absorption coefficients, which make them suitable as photoactive semiconductors for harvesting the visible light of the solar spectrum [4–6]. FeS$_2$ was employed for the photocatalytic degradation of several organic pollutants, such as methylene blue, rhodamine B and methyl orange [7], rose Bengal [8], reactive black 5 and reactive orange 4 [9], and phenol [10]. CuS was used for the degradation of methylene blue and rhodamine B [11–13], eosin Y and congo red [14]; while NiS$_2$ efficiently removed crystal violet, rhodamine B, methylene blue, eriochrome black T [15], erythrosine and phenol red [16].

Indigo carmine is a non-biodegradable dye commonly present in waste water derived from textile industries, and it is also employed in food coloring processes and as indicator in analytical methods [17, 18]. Due to the toxic and carcinogen nature of indigo carmine, the removal of this and other related dyes from waste water is a major environmental problem [19]. Traditional methods (adsorption, biodegradation, etc.) are usually ineffective and of high cost [20]. For this reason, in this work we propose for the first time the

utilization of FeS_2, CuS, and NiS_2 as photocatalysts for the degradation of indigo carmine.

Other applications of these metal sulfides include lithium-ion batteries, supercapacitors, dye-sensitized solar cells, photodetectors [21–26], and as electrocatalysts for the hydrogen evolution reaction (HER) [26–29]. For the photocatalytic hydrogen generation reaction, these materials were used mainly as cocatalysts or coupled to wide band gap semiconductors, using triethanolamine and Na_2S–Na_2SO_3 as sacrificial reagents [30, 31]. Other sacrificial reagents that have promoted a significant enhancement in the photocatalytic activity for hydrogen evolution over oxide semiconductors are EDTA, alcohols, and $NaIO_3$–NaI [32]. Due to the negative value of their conduction bands, in recent days a variety of metal sulfides including MoS_2, CuS, NiS, NiS_2, and FeS_2 have been studied for photo and electrocatalytic carbon dioxide reduction [33–36].

In this work, we study the photocatalytic properties of FeS_2, CuS, and NiS_2 for the hydrogen evolution reaction. Metal sulfides can be obtained by several techniques such as solvothermal synthesis [37], sonochemistry [38] and pyrolysis [39]. However, an adequate optimization of the synthesis conditions to control the stoichiometry and crystalline structure of the phases is still a challenge and the above mentioned methods employ difficult conditions such as high temperature, long time of reaction and toxic precursors (for example, H_2S) [40], and usually result in low yields; which is not appropriate for large scale production [41]. The advantage of the hydrothermal synthesis proposed herein includes the obtention at low temperature (150 °C), short time (4 h) and with high yield (> 93%) of the pure phases of metal sulfides. Additionally, pH control is not needed, and no complexing agents are used. Therefore, there are no release of undesired products and the method is environmentally friendly. These features describe the principles of the green chemistry approach [42].

Moreover, a comparative study of the photocatalytic activity for hydrogen evolution and indigo carmine dye degradation over the as-prepared metal sulfides is presented. The stability and electrical properties of the materials are discussed through electrochemical analysis, and three sacrificial reagents of different nature (inorganic salt, organic acid, and alcohol) are evaluated to enhance the activity of the materials for H_2 evolution.

2 Experimental

2.1 Synthesis of metal sulfides by hydrothermal method

Stoichiometric amounts of the transition metal salts ($Fe(NO_3)_3 \cdot 9H_2O$, $Cu(NO_3)_2 \cdot 3H_2O$, and $Ni(NO_3)_2 \cdot 6H_2O$,

Sigma Aldrich 99.95%) and sodium thiosulfate ($Na_2S_2O_3 \cdot 5H_2O$, Sigma Aldrich 99.5%) were dissolved in 15 mL of deionized water and stirred during 20 min. The solutions were mixed and transferred into a 40 mL Teflon autoclave reactor and heated at 150 °C for 4 h in a furnace. After this time, the reactor was removed from the furnace and cooled to ambient temperature. The solution was centrifuged to separate the solid product. Then, the obtained powder was washed 5 times with water and dried in air at 70 °C. This procedure is illustrated in Fig. 1.

2.2 Characterization of samples

The analysis of the crystalline structure of the materials was performed by X-ray diffraction (XRD) in a Bruker D8 Advance diffractometer operating at 40 kV and 40 mA with CuKα radiation ($\lambda = 1.5406$ Å), in a 2θ range of 10°–70° with a scan rate of 0.05°. The Scherrer equation was employed to calculate the crystallite size of the samples: $L = \kappa\lambda/\beta\cos(\theta)$ [43]. In this equation, L represents the crystallite size, κ the Scherrer constant (0.89), λ the wavelength of the X-ray radiation (0.15418 nm for CuKα) and β the full width at half maximum of the diffraction peak at 2θ. The surface morphology and elemental composition of the metal sulfides were studied in a scanning electron microscope (SEM-JEOL 6490LV) coupled with an energy dispersive X-ray spectroscopy (EDS) analyzer using 20 kV of voltage. The average particle size was calculated from SEM images using the software ImageJ. Band gaps of the materials were estimated by UV–Vis diffuse reflectance spectroscopy, using a Cary 5000 UV–Vis NIR spectrophotometer with $BaSO_4$ as standard. From the diffuse reflectance data, the Tauc plot was obtained, and the band gaps (E_g) were estimated extrapolating the absorption onset to the x-axis. The conduction and valence band of the metal sulfides were theoretically estimated through the equation $E_{VB} = EN - E^e + 0.5 \times E_g$ [44], where E_{VB} is the valence band, EN the electronegativity of the semiconductor, E^e the energy of free electrons on the hydrogen scale (~ 4.5 eV), and E_g the band gap. E_{CB} is the potential of the conduction band and can be obtained by the relation: $E_{CB} = E_{VB} - E_g$ [44]. To study the recombination
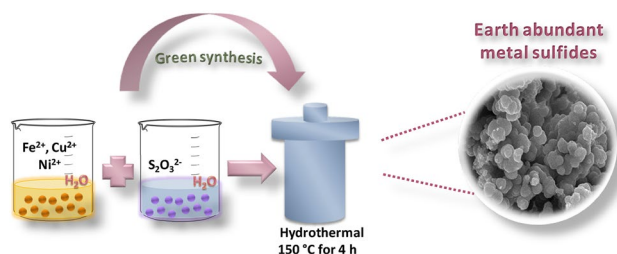

Fig. 1 Schematic illustration of the hydrothermal synthesis of FeS_2, CuS, and NiS_2 powders

in the samples, photoluminescence analysis was performed in an Agilent Cary Eclipse fluorescence spectrophotometer, with a scanning speed of 1000 nm min^{-1} and an excitation wavelength of 689 nm. The surface area and pore diameter of the samples were estimated using a BELSORP mini II (BEL Japan), by the Brunauer–Emmet–Teller (BET) and Barrett–Joyner–Halenda (BJH) method. Before the analysis, the samples were degassed for 3 h at 70 °C.

2.3 Electrochemical characterization

For the electrochemical characterization, working electrodes were prepared from the powdered metal sulfides. To form a suspension, 5 mg of the metal sulfides and 50 µL of Nafion® (5% in a mixture of alcohol and water, Aldrich) were dispersed in 30 µL of ethanol and 420 µL of deionized water. The suspension was ultrasonicated for 10 min. After that, 6 µL suspension was deposited on a carbon paper substrate (Sigracet®, electric resistivity < 15 mΩ cm^2) with an active area of 1×2 cm^2 by the drop-casting method. In this process, the suspension was placed on the lower part of the carbon paper. Next, the electrodes were dried at 60 °C in an oven for 30 min. Afterwards, ohmic electric contacts were attached with silver paste and copper wire on the undeposited area of the substrate; then, the contact was covered with non-conducting epoxy resin. The electrochemical measurements were performed in a three-electrode H-type glass cell with a glass frit to separate the working and counter electrode compartments. The analysis was run by a potentiostat (Gamry Ref600) and the electrodes prepared of metal sulfides on carbon paper were used as working electrode while a Pt wire and a Ag/AgCl were used as counter and reference electrode, respectively.

Cyclic voltammetry and Mott–Schottky measurements were performed under dark conditions in a potential range of 0.8 to -0.8 V$_{RHE}$ at a scan rate of 20 mV s^{-1} in a 0.5 H$_2$SO$_4$ electrolyte (pH 0). The current density was calculated considering the area of the electrode: J = current/area of the electrode (1.5 cm^{-2}). Electrochemical impedance spectroscopy analysis was carried out under dark in open circuit conditions at a frequency range of 100 kHz–100 MHz and an AC perturbation of 10 mV. The potential versus Ag/AgCl, $E_{Ag/AgCl}$, was converted to reversible hydrogen electrode potential, E_{RHE}, using the Nernst equation: $E_{RHE} = E_{Ag/AgCl} + E^0_{Ag/AgCl} + 0.059 \times pH$, where $E^0_{Ag/AgCl} = 0.1976$ V at 25 °C [45, 46].

2.4 Photocatalytic tests

The photocatalytic activity for hydrogen evolution was tested in a 250 mL Pyrex reactor, dispersing 0.2 g of the sample in 200 mL of water. Nitrogen gas was employed to deaerate the media. The reactor was illuminated with simulated solar light (AM 1.5G) with a 450 W Xe-lamp. The hydrogen evolution was analyzed online every 30 min for 3 h in a gas chromatograph (Thermo Scientific) with a TCD detector and fused silica capillary column. For the hydrogen evolution tests in the presence of sacrificial reagents, solutions of Na$_2$S/Na$_2$SO$_3$ (0.35/0.25 M), EDTA (10% w/v), and ethanol (10% v) were used as reaction media and the rest of the experiment proceeded under identical conditions. For the preparation of EDTA (10% w/v) and ethanol (10% v/v) solutions, 20 g of ethylenediaminetetraacetic acid disodium salt (99.0% Sigma Aldrich) and 20 mL of ethanol (analytical grade, Sigma Aldrich) were dissolved in 200 mL of distilled water. In the case of Na$_2$S/Na$_2$SO$_3$ (0.35/0.25 M), 16.8 g of sodium sulfide hydrate (Na$_2$S·9H$_2$O 98% Sigma Aldrich) and 6.3 g of anhydrous sodium sulfate (Na$_2$SO$_3$ 98% Sigma Aldrich) were dissolved in 200 mL of distilled water. The concentrations of Na$_2$S/Na$_2$SO$_3$ (0.35/0.25 M) and ethanol (10% v/v) were selected according to the optimal concentration reported in literature of these sacrifice agents [47]. Regarding EDTA, a concentration of 10% w/v was used due to at higher concentrations the solubility of EDTA is limited.

The photocatalytic activity of the metal sulfides for the degradation of indigo carmine dye (indigo-5,5′-disulfonic acid disodium salt), was studied under irradiation of the same solar simulator used in the hydrogen evolution tests. For the experiment, 0.2 g of photocatalyst was dispersed in 200 mL of a solution 30 ppm of indigo carmine and transferred into the glass reactor. The solution was kept under dark for 1 h to reach the adsorption equilibrium. After that, the illumination started, and the kinetic of the reaction was studied taking aliquots of the reactor every 30 min. The concentration of the colorant was determined using a UV–Vis spectrophotometer (Perkin Elmer, Lambda 35), analyzing the absorbance at 611 nm. In some of the results below, indigo carmine is abbreviated as IC.

3 Results and discussion

3.1 X-ray diffraction

Figure 2 shows the X-ray powder diffraction patterns of the synthesized metal sulfides. The diffraction patterns of the samples are indexed to *pyrite* FeS$_2$ (JCPDS: 01-079-0617), *covellite* CuS (JCPDS: 06-0464), and *vaesite* NiS$_2$ (JCPDS: 01-089-7142). No additional peaks are observed, confirming the purity of the phases. Cubic FeS$_2$ and NiS$_2$ are isostructural phases with similar lattice constants, and their XRD patterns are very similar, while CuS crystallized in a hexagonal symmetry. Through the Scherrer equation, the crystallite size of the materials is estimated, taking the average of the 5 most intense peaks of each phase. FeS$_2$ shows
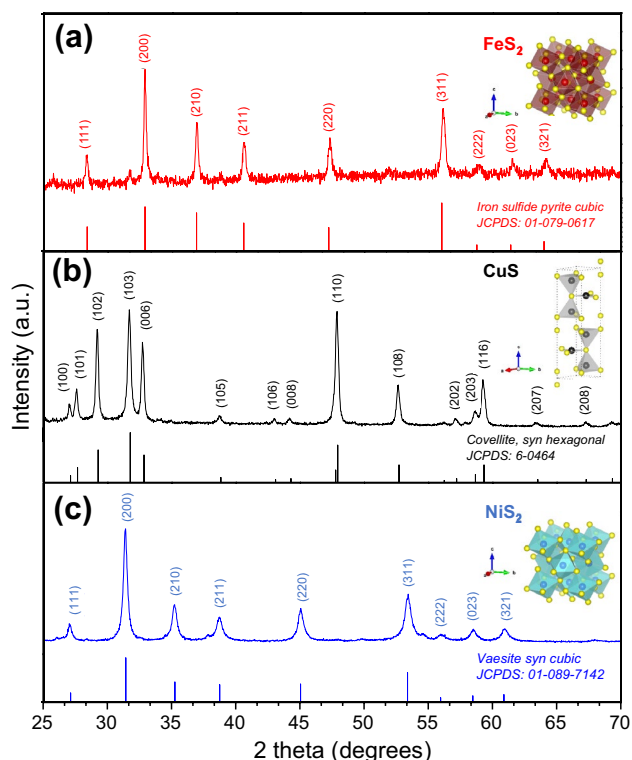
Fig. 2 XRD diffraction patterns and schematic representations of the crystalline structure of **a** FeS$_2$, **b** CuS and **c** NiS$_2$

a crystallite size of 50 nm, while CuS and NiS$_2$ show 45 and 22 nm, respectively. In a semiconductor photocatalyst, a higher crystallinity typically allows a better charge transport in the structure, reducing the recombination and increasing the efficiency of the photocatalytic reaction [48].

3.2 Scanning electron microscopy

Scanning electron microscopy images and EDS analysis of the samples are shown in Fig. 3a–f. The morphological exploration shows that the as-prepared sulfides are formed of agglomerates of particles. For the FeS$_2$ sample, polyhedral particles of ~676 ± 44 nm are observed; while in the case of CuS and NiS$_2$, irregular and spherical shaped particles of around ~783 ± 53 and 933 ± 68 nm are identified. These values represent an average particle size determined by counting 300 particles using Image J software.

All the samples exhibit uniform morphology and particle size distribution, attributed to a controlled growth during the hydrothermal synthesis. A small particle size is favorable for the photocatalytic process, allowing a short transport distance of the photogenerated charges from the bulk to the surface, where the redox reactions take place [48]. An EDX analysis of the surface of the metal sulfides confirms the presence of iron, copper, nickel, sulfur, and carbon, in agreement with the purity of the phases observed by XRD. The

carbon signal is attributed to carbon tape, used to support the powder samples on the stainless steel SEM holder. The theoretical and experimental composition of the samples in atomic % determined by EDX is presented in Table 1. For the quantification, the carbon signal was not taken into account. According to these results, the atomic content of Fe, Cu, Ni, and S in the samples is in agreement with the theoretical atomic % in all the phases.

3.3 UV–Vis diffuse reflectance spectroscopy

The optical band gaps of the metal sulfides prepared by hydrothermal method are determined from the absorbance spectra (Fig. 4). From these curves, the band gap values were estimated. The values obtained for FeS$_2$, CuS and NiS$_2$ are 1.4, 1.8, and 1.3 eV, respectively. These values are in good agreement with values reported in previous works [49–51]. As can be observed in Fig. 4, all the metal sulfides show high absorption in the visible region (400–800 nm). This is a desirable property in the photocatalysts since the solar spectrum is dominated by visible light (45%) [52]. The relatively small band gaps of FeS$_2$, CuS, and NiS$_2$ (1.3–1.8 eV), imply that these materials can absorb much of the photons in the visible range and produce electron–hole pairs, which can participate in different redox reactions.

3.4 Physisorption analysis

Isotherms of FeS$_2$, CuS, and NiS$_2$ are presented in Fig. 5a–c. The pore size distribution is showed in the inset graph. The calculated specific surface areas of FeS$_2$, CuS, and NiS$_2$ are 4, 3, and 14 m^2 g^{-1}, respectively, and their pore diameter values are 20, 17, and 23 nm. These values are presented in Table 2, along with a summary of the structural and optical properties of the materials. According to IUPAC recommendation, materials having pore diameter in the range of 2–50 nm are considered mesoporous and loop in adsorption desorption depends on types of pore [53, 54]. The loop for FeS$_2$ and NiS$_2$ is type IV which is characteristic for bottleneck pores, while for CuS the loop is type II, corresponding to capillary pores [55–58].

3.5 Photoluminescence analysis

Photoluminescence spectroscopy (PL) is a powerful technique to study the band gap energy, electronic structure, and defects in semiconductors [58]. The PL emission is associated with the recombination of an electron–hole pair, which liberates a photon. A higher PL emission intensity implies a higher recombination rate and short lifetime of the excitons [59]. Figure 6 presents the photoluminescence spectra of FeS$_2$, CuS, and NiS$_2$, obtained at room temperature. The materials present a strong emission centered at ~840, 692,
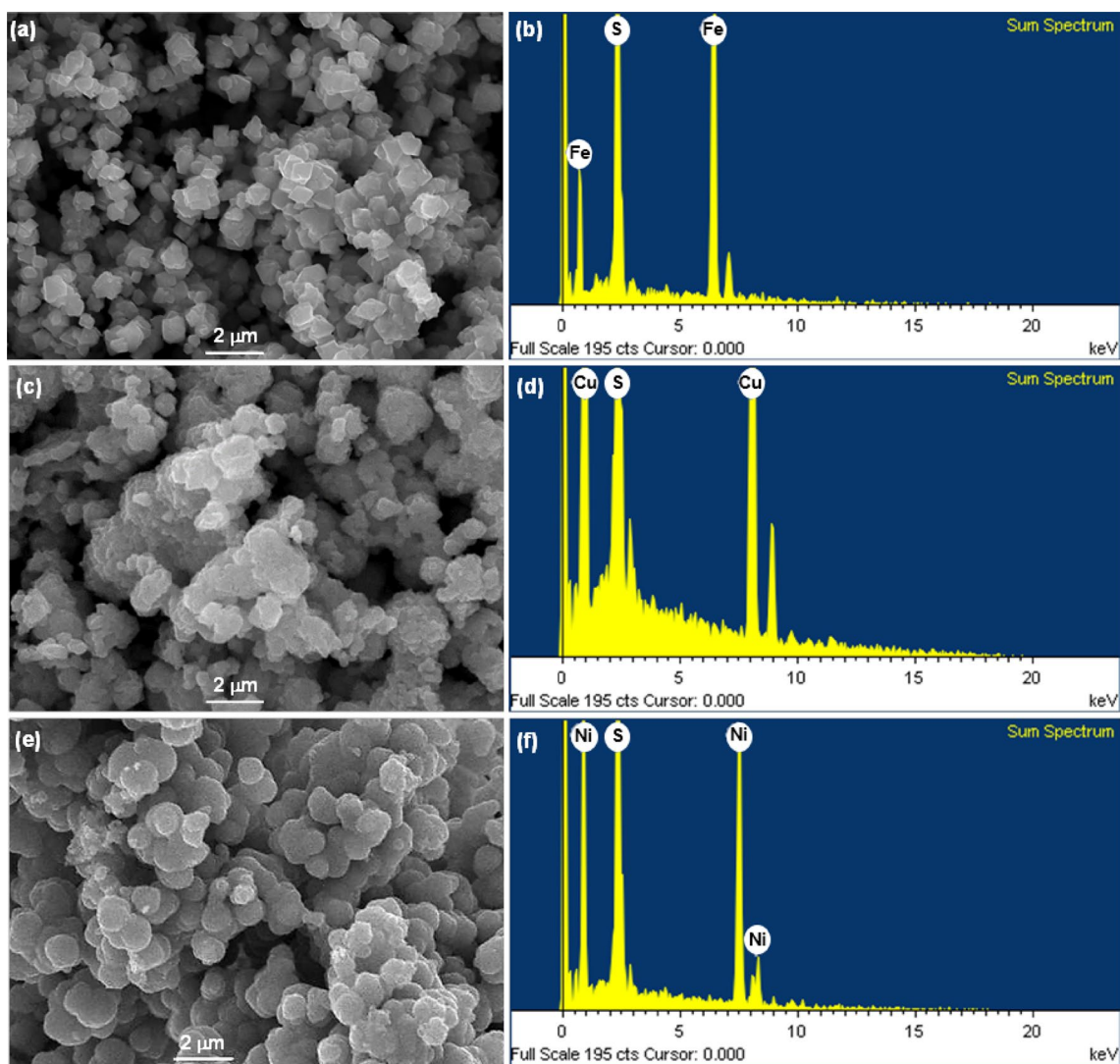
Fig. 3 SEM and EDS analysis of **a, b** FeS_2, **c, d** CuS and **e, f** NiS_2

Table 1 Theoretical and experimental composition of the samples FeS_2, CuS, and NiS_2 determined by EDX

Material	Elemental composition	Theoretical atomic %	Experimental atomic % determined by EDX
FeS_2	Fe	33.3	30.8
	S	66.7	69.2
CuS	Cu	50.0	47.6
	S	50.0	52.4
NiS_2	Ni	33.3	31.5
	S	66.7	68.5

Fig. 4 Absorbance spectra of the hydrothermal synthesized samples (*a*) FeS_2, (*b*) CuS, and (*c*) NiS_2

and 825 nm for FeS_2, CuS, and NiS_2, respectively, related to the band to band transition occurring during the recombination of the electron–hole pairs. According to this graph, FeS_2 exhibits the lower PL intensity, corresponding to a low
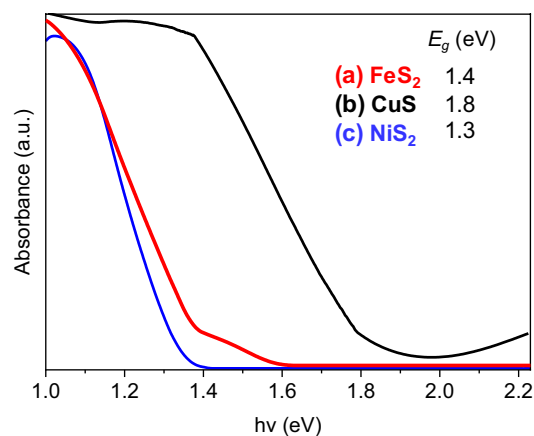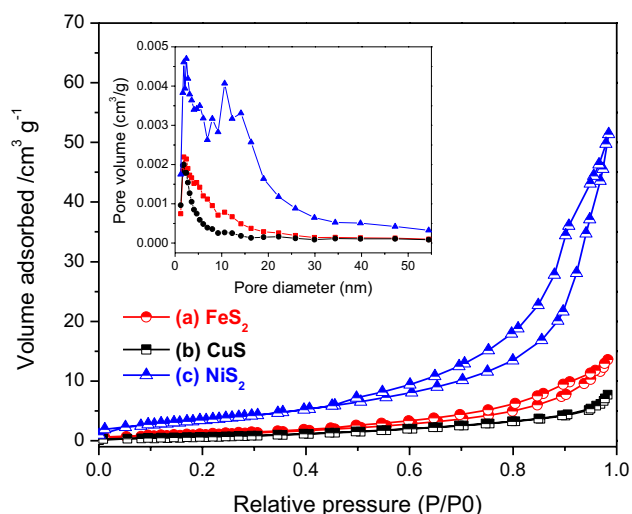
Fig. 5 N_2 adsorption–desorption isotherms and pore size distribution of (*a*) FeS_2, (*b*) CuS and (*c*) NiS_2. The pore size distribution is included in the inset graph

Table 2 Summary of the structural, optical and textural properties of the photocatalysts

Sample	Band gap (eV)	Average particle size (nm)	S_{BET} $(m^2 g^{-1})$	Pore diameter (nm)	Crystallite size (nm) D
FeS_2	1.4	676	4	20	50
CuS	1.8	783	3	17	45
NiS_2	1.3	933	14	23	22

recombination rate. NiS_2 exhibits the highest recombination rate. FeS_2 is the material with the smallest average particle size (676 nm) and the highest crystallite size (50 nm), compared to CuS and NiS_2. A small particle size reduces the diffusion path of the charge carriers to the surface, decreasing the probability of recombination; while a high crystallite size indicates an appropriate crystal growth and a reduced amount of defects in the material, promoting a better charge transport and utilization [48]. Therefore, from this analysis, it is expected that FeS_2 and NiS_2 show the highest and lowest photocatalytic activity, respectively.

3.6 Electrochemical characterization

Electrochemical impedance spectroscopy analysis is performed in this work to study the charge transfer properties in the semiconductors. Figure 7 presents the Nyquist plots obtained in dark conditions. From this figure, it is observed that the FeS_2 sample exhibits a larger radius of the main semicircle, followed by CuS, and the smallest semicircle is presented by NiS_2. These results suggest that NiS_2 exhibit a better electron transfer between electrode/electrolyte,
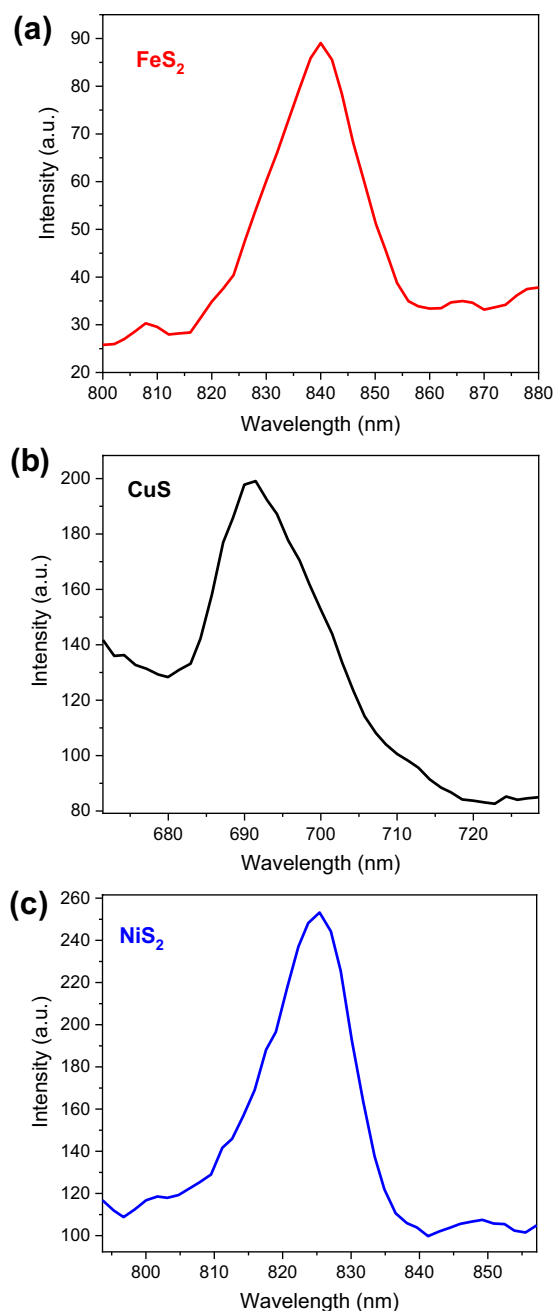

Fig. 6 Photoluminescence spectra of **a** FeS_2, **b** CuS and **c** NiS_2

compared to the other sulfides, considering that a small semicircle radius involves a faster charge transfer [60].

The Mott–Schottky plots (Fig. 8) of the samples show a positive slope, confirming the n-type conductivity of the metal sulfides. The flat band potential of the semiconductors, V_{fb}, is estimated from the intercept at the x-axis of the linear fitting of the plot, and the donor density, N_d, from the slope and the values are summarized in Table 3. From this analysis, it is observed that FeS_2 exhibits the more negative flat band potential (-0.35 V_{RHE}), followed by NiS_2 (-0.32
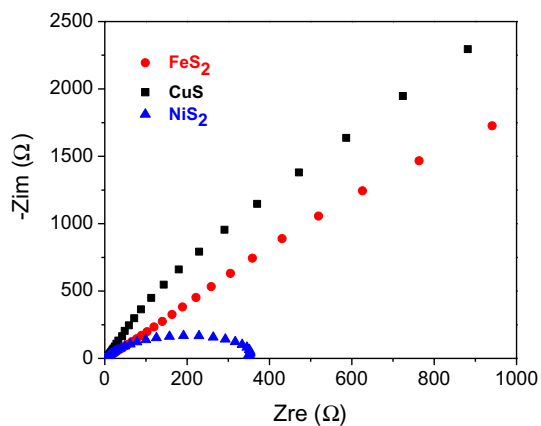
Fig. 7 Nyquist plots obtained in the dark at E = 0.4 V_{RHE} with AC perturbation of ± 10 mV, for FeS_2, CuS, and NiS_2
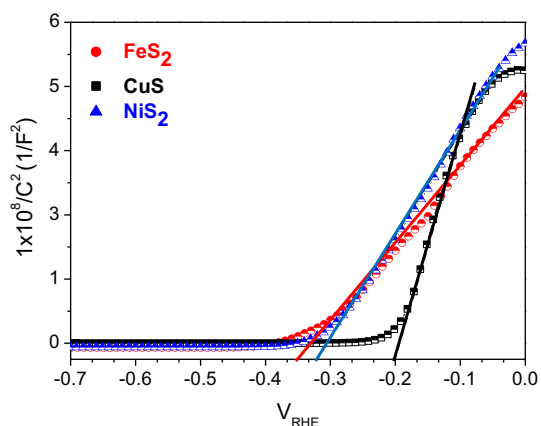

Fig. 8 Mott–Schottky plots of the samples indicated in the figure. The solid lines represent the slope considered to estimate the flat band potential

Table 3 Properties of the semiconductors estimated from Mott–Schottky analysis

Material	Conductivity type	Flat band potential V_{fb} (V_{RHE})	Donor density N_d (cm^{-3})
FeS_2	N	− 0.35	1.27×10^{17}
CuS	N	− 0.20	5.63×10^{19}
NiS_2	N	− 0.32	1.20×10^{17}

V_{RHE}) and CuS (− 0.20 V_{RHE}). The flat band potential is related to the photocatalytic activity of the material, and a more negative value implies a higher capacity of the material to perform the separation of the photogenerated charges [61].

The donor density in the samples varies from 1.27×10^{17} and 1.20×10^{17} (for FeS_2 and NiS_2, respectively) to 5.63×10^{19} (for CuS). A higher donor density involves
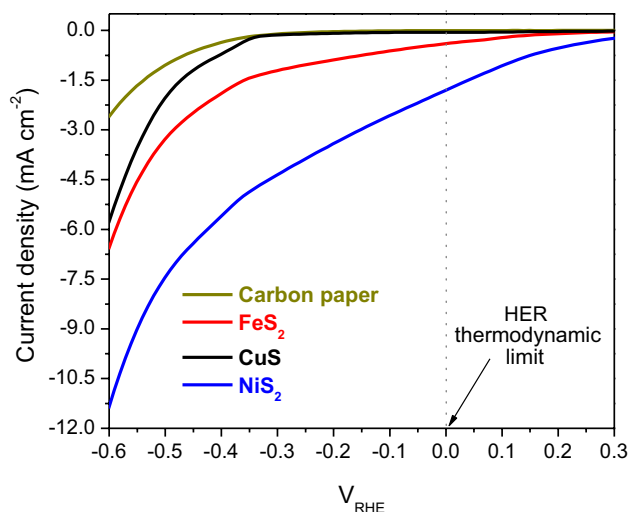

Fig. 9 Current–potential curves of FeS_2, CuS, and NiS_2

a major concentration of carriers in the sample and an enhanced conductivity, which is positive for the effective transport and utilization of the charges in the photocatalytic processes [62].

According to the values obtained of the charge carrier concentration, the expected activity should be: CuS > FeS_2 > NiS_2, but taking in account the estimated flat band potential values, the predicted catalytic activity should follow the tendency: FeS_2 > NiS_2 > CuS.

However, even when CuS exhibit the highest charge carrier concentration compared to FeS_2 and NiS_2, as it will be shown in the "Photocatalytic activity" section, the more negative value of the flat band potential in iron and nickel sulfides seems to play a more determinant role in the charge separation and transport processes, promoting a higher activity in FeS_2. In the case of NiS_2, the activity is limited due to the low potential value of the valence band, making the NiS_2 susceptible to be oxidized by the photogenerated holes, which diminishes the overall photocatalytic efficiency.

Cyclic voltammetry studies were performed to evaluate the activity for the hydrogen evolution reaction (HER) of the samples in dark conditions without sacrificial agents (Fig. 9). The curve of the carbon paper used as substrate is included for reference. As can be observed in this figure, the FeS_2 and CuS electrodes show negligible current in the cathodic scan until about the onset of the HER reaction (− 0.34 V_{RHE}) (see Fig. S1, in Supporting information for more details of the calculation of the onset potential). The cyclic voltammetry analysis show the suitability of these materials to work as electrocatalysts for the (HER), and there is no large difference in their activity. The onset potential of the metal sulfides developed in this work (− 0.34 V_{RHE}) is quite high compared to MoS_2 (− 0.16 V_{RHE}) [63], a material with high activity for HER. However, as the FeS_2, CuS, and

NiS_2 are cheap and abundant materials they might still be interesting materials in the search for platinum group metal (PGM) free catalysts for HER [64, 65]. Moreover, the activity of these materials for HER can be further improved by e.g. changing the material structure.

For the NiS_2 sample it is clear that a negative current (i.e. a reduction reaction) starts already at positive potentials (about 0.2 V_{RHE} in the cathodic scan). As this potential is more positive than the required for HER (0 V_{RHE}), this current must originate from a reduction reaction in the electrode material, i.e. the NiS_2. The curves presented in Fig. 9 correspond to the cycle 10 of the cyclic voltammetry measurement of every sample. The rest of the samples are included in Supporting Information (Fig. S2). The successive cyclic voltammetry scans show the electrochemical stability of the samples after several cycles.

3.7 Photocatalytic activity

3.7.1 Hydrogen evolution

Figure 10 presents the potentials of the conduction and valence bands of the metal sulfides compared with the potentials of reduction and oxidation of water. As can be observed in this figure, all the materials are active under visible light and exhibit a conduction band more negative than 0 V_{RHE}. Therefore, they are able to perform the reduction of water. From this diagram, a more negative potential of the conduction band promotes a higher rate of the water reduction reaction. The valence bands of FeS_2 and CuS are very near and more positive than 1.23 V_{RHE}, respectively. For the oxygen evolution reaction (OER) a minimum theoretical potential of 1.23 V_{RHE} is required, however, experimentally, an overpotential is required.
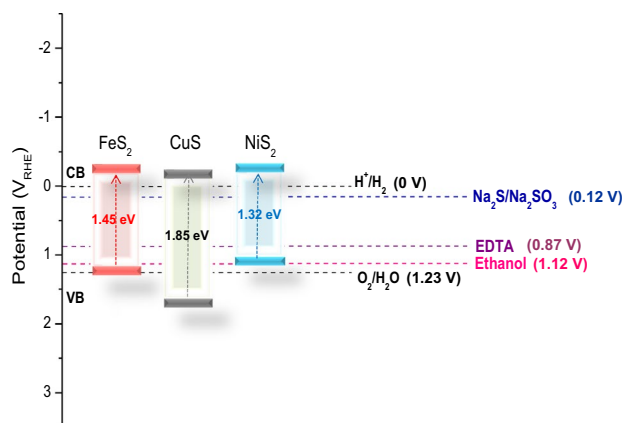

Fig. 10 Energy band diagram of FeS_2, CuS and NiS_2 photocatalysts compared with **a** the oxidation and reduction potential of water and the oxidation potential of the sacrificial agents Na_2S/Na_2SO_3, EDTA, and ethanol [66]

In the case of NiS_2, the valence band is less positive than the oxidation potential of water. Due to this, the NiS_2 should not be able to perform the oxidation of water.

The photocatalytic hydrogen evolution over the metal sulfides under simulated solar irradiation is presented in Fig. 11. As can be seen in this figure, the materials show a constant hydrogen production. The H_2 evolution rates, calculated from the slope of the plot, are 32, 14, and 8 µmol g^{-1} h^{-1} for FeS_2, CuS, and NiS_2, respectively. FeS_2 exhibits the largest crystallite size (50 nm), the smaller particle size (676 nm), the most negative value of the flat band potential (−0.35 V_{RHE}), and the lowest recombination in the photoluminescence analysis. These features should give this material an enhanced charge separation and transport, leading to a higher photocatalytic efficiency. The lowest activity is presented by NiS_2, which could be associated with the oxidation of this semiconductor, as discussed in the electrochemical section.

Figure 10 also includes the oxidation potentials of three different sacrificial reagents: an inorganic salt (Na_2S/Na_2SO_3), an organic acid (EDTA), and an alcohol (ethanol), which are employed in the tests for the photocatalytic hydrogen evolution to evaluate the effect on the catalytic activity. The values of the oxidation potential of the sacrificial reagents were taken from the work of Wang et al. [66], where cyclic voltammetry studies were performed to estimate these values from the oxidation peak. The anodic peak is related to the first step in the oxidation of the organic molecule.

The three sacrificial reagents have an oxidation potential less positive than water, so the photogenerated holes participate in the oxidation of these compounds, while the electrons are available to perform the reduction of water. In this way, the recombination of charges is reduced.

The results of the photocatalytic activity of the metal sulfides in the presence of Na_2S/Na_2SO_3, EDTA, and ethanol are shown in Fig. 11. As observed in this figure, when using Na_2S/Na_2SO_3 as sacrificial reagent, the activity for H_2 evolution increases more than 15 times compared to pure water. The use of EDTA increases the activity of the materials more than 6 times, and the lower enhancement effect is produced by ethanol, which promotes an increase by only 3 times. These results suggest that the higher hydrogen evolution rate promoted by Na_2S/Na_2SO_3 is associated with the lower oxidation potential compared to EDTA and ethanol. These results are summarized in Fig. 12 and Table 4.

A mechanism of the photocatalytic reaction in the presence of the sacrificial reagents is presented in Fig. 13. The reactions presented in this figure are based in mechanisms reported by several authors [66–68]. According to this, after the irradiation of the metal sulfide with simulated solar irradiation and the generation of the electron–hole pairs, the electrons participate in the reduction of protons to evolve hydrogen gas. The holes are used in the oxidation of the
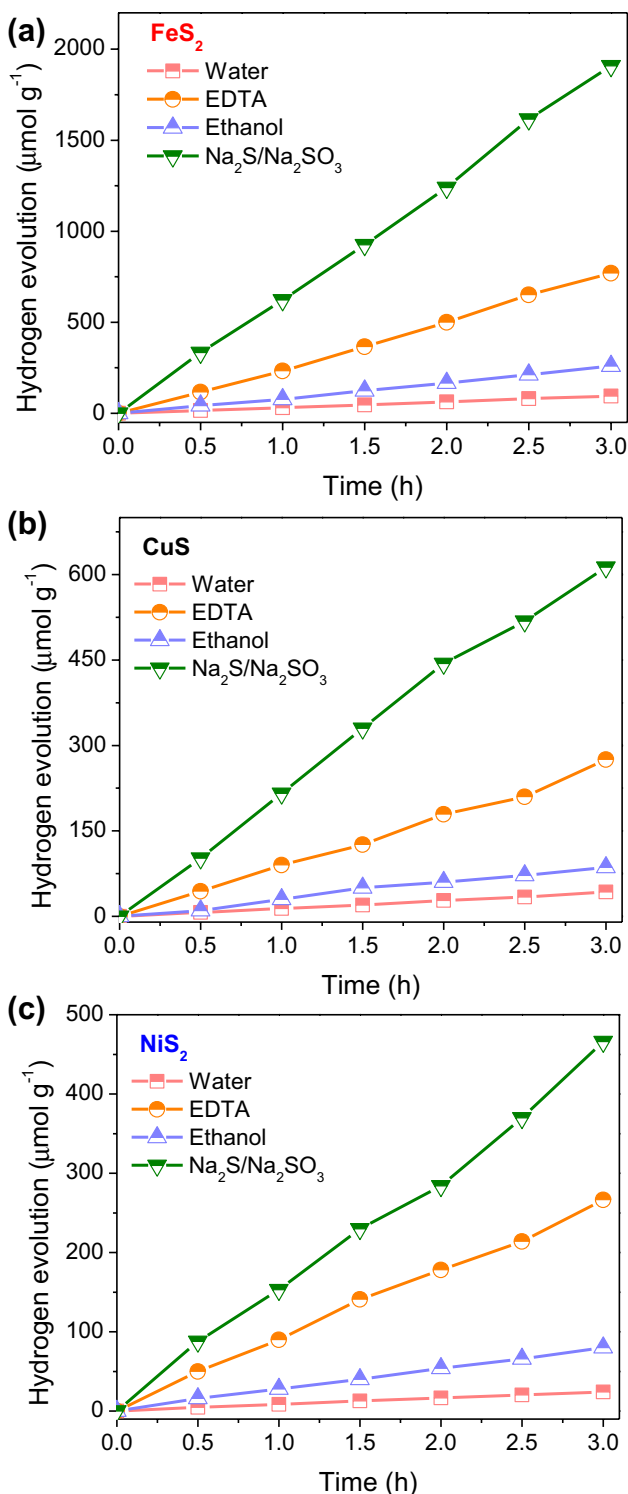
(a) FeS$_2$
- Water
- EDTA
- Ethanol
- Na$_2$S/Na$_2$SO$_3$

(b) CuS
- Water
- EDTA
- Ethanol
- Na$_2$S/Na$_2$SO$_3$

(c) NiS$_2$
- Water
- EDTA
- Ethanol
- Na$_2$S/Na$_2$SO$_3$

Fig. 11 Photocatalytic hydrogen evolution over **a** FeS$_2$, **b** CuS, and **c** NiS$_2$, under simulated solar irradiation and using different sacrificial reagents

Fig. 12 Average hydrogen evolution over the metal sulfides studied in this work in pure water and in the presence of three different sacrificial reagents

Table 4 Summary of the hydrogen evolution rate over the metal sulfides FeS$_2$, CuS, and NiS$_2$ in the presence of different sacrificial agents

Sacrificial agent	Hydrogen evolution rate (μmol g^{-1} h^{-1})		
	FeS$_2$	CuS	NiS$_2$
Water	32	14	8
EDTA	260	89	55
Ethanol	86	29	26
Na$_2$S/Na$_2$SO$_3$	636	207	149

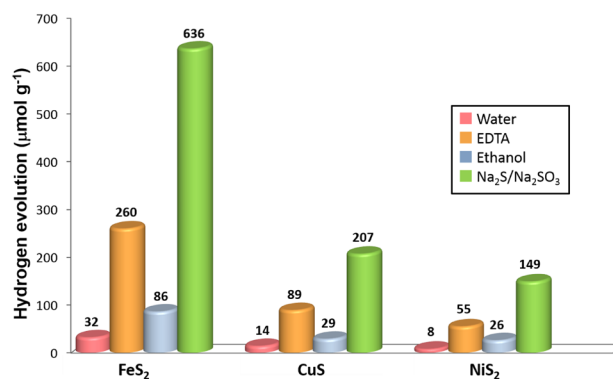sacrificial agents, reducing the recombination of the photogenerated charges and improving the photocatalytic activity. From this, we suggest the oxidation is the limiting step from the reaction. Thus, adding a sacrificial agent that is easier to oxidize than water increase the hydrogen evolution efficiency.
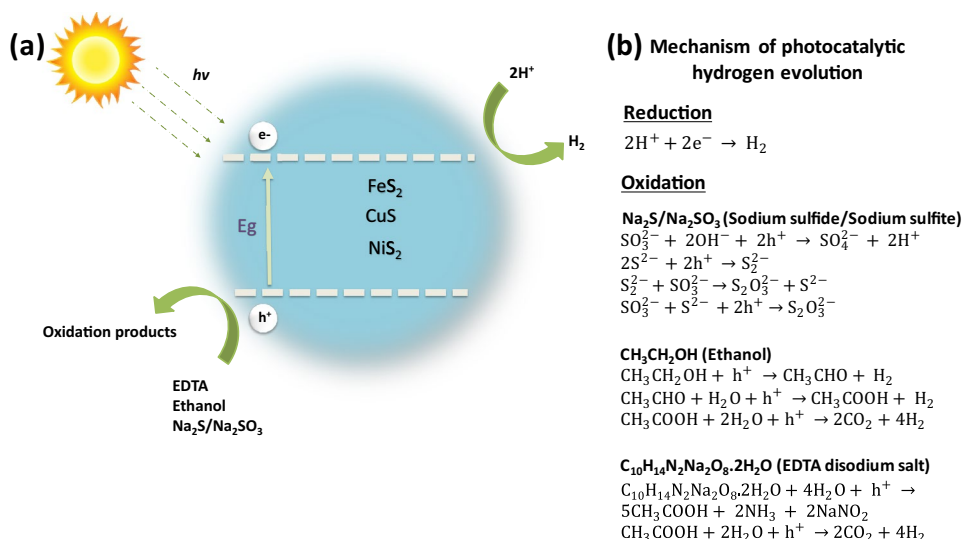
3.8 Degradation of indigo carmine dye

The metal sulfides are also evaluated in this work for the photocatalytic degradation of indigo carmine.

In photocatalytic degradation, commonly the active species are electrons, holes, hydroxyl ($^{\cdot}$OH) and superoxide (O$_2$$^{\cdot-}$) radicals. In Fig. 14 we present the CB and VB energies of the metal sulfides compared to the required potential to generate the radicals O$_2$$^{\cdot-}$ (− 0.046 V$_{RHE}$) and $^{\cdot}$OH (1.99 V$_{RHE}$) [69]. According to this diagram, the sulfides should be capable of producing O$_2$$^{\cdot-}$ radicals, and along with the photogenerated electron and holes, we suggest they are the main species involved in the degradation of indigo carmine dye. We also include in this diagram the potentials of oxidation (0.84 V$_{RHE}$) and reduction (0.25 V$_{RHE}$) of indigo carmine dye at pH 7 [70]. From this Figure, the oxidation and reduction of the indigo carmine molecule is factible over the studied photocatalysts.

Figure 15a shows the change in the concentration of the dye and Fig. 15b shows ln(C$_0$/C) as a function of the time

Fig. 13 Process of **a** photoexcitation and **b** mechanism of photocatalytic hydrogen evolution over FeS_2, CuS and NiS_2 in the presence of sacrificial reagents, and under simulated solar irradiation

(b) Mechanism of photocatalytic hydrogen evolution

Reduction
$$2H^+ + 2e^- \rightarrow H_2$$

Oxidation

Na_2S/Na_2SO_3 (Sodium sulfide/Sodium sulfite)
$$SO_3^{2-} + 2OH^- + 2h^+ \rightarrow SO_4^{2-} + 2H^+$$
$$2S^{2-} + 2h^+ \rightarrow S_2^{2-}$$
$$S_2^{2-} + SO_3^{2-} \rightarrow S_2O_3^{2-} + S^{2-}$$
$$SO_3^{2-} + S^{2-} + 2h^+ \rightarrow S_2O_3^{2-}$$

CH_3CH_2OH (Ethanol)
$$CH_3CH_2OH + h^+ \rightarrow CH_3CHO + H_2$$
$$CH_3CHO + H_2O + h^+ \rightarrow CH_3COOH + H_2$$
$$CH_3COOH + 2H_2O + h^+ \rightarrow 2CO_2 + 4H_2$$

$C_{10}H_{14}N_2Na_2O_8 \cdot 2H_2O$ (EDTA disodium salt)
$$C_{10}H_{14}N_2Na_2O_8 \cdot 2H_2O + 4H_2O + h^+ \rightarrow$$
$$5CH_3COOH + 2NH_3 + 2NaNO_2$$
$$CH_3COOH + 2H_2O + h^+ \rightarrow 2CO_2 + 4H_2$$

of irradiation. FeS_2 exhibits 88% of indigo carmine degradation under visible light, followed by CuS (78%) and NiS_2 (51%). The catalytic activity for indigo carmine degradation shows the same tendency compared to the hydrogen production: $FeS_2 > CuS > NiS_2$, also adjudicating the higher activity of FeS_2 to its higher crystallinity, lower particle size, and lower recombination, promoting an enhanced charge carrier dynamics of separation, migration, and utilization, and an improved photocatalytic activity. Table 5 summarizes the percentages and rate constants of degradation obtained from the photocatalytic tests.
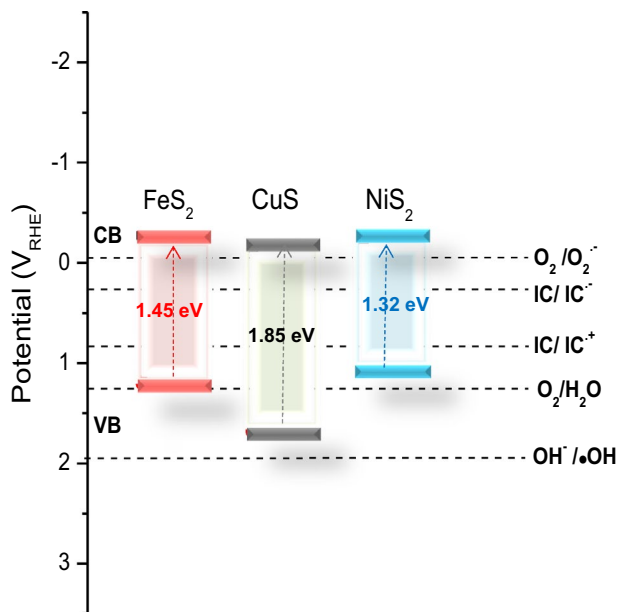

Fig. 14 Energy band diagram of FeS_2, CuS and NiS_2 photocatalysts compared with the required potentials for the formation of the main species involved in degradation

A mechanism of the photocatalytic degradation of indigo carmine is presented in Fig. 16. In the proposed mechanism, the metal sulfides are excited with visible light and photogenerated charges (electron and hole) migrate from the bulk to the surface of the photocatalyst. After that, the electrons react with the dissolved oxygen in the solution, leading to the formation of superoxide radicals. Superoxide radicals attack the organic dye, promoting its oxidation for obtaining derived low molecular weight molecules.

According to Fig. 14, in FeS_2 and CuS the photogenerated holes lack from the required potential to produce hydroxyl radical. Therefore, the holes oxidize water molecules to produce O_2, which is reduced by electrons to form additional superoxide radicals that participate in the oxidation of the organic dye. In the case of NiS_2, the electrons in the conduction band have the potential to produce superoxide radicals and promote the degradation of the indigo carmine dye, but the holes in the valence band are not able to oxidize water. In this case, the holes produced from the photoexcitation oxidize NiS_2.

4 Conclusions

In this work, we obtained the pure phases of FeS_2, CuS, and NiS_2 at low temperature and short time (150 °C for 4 h) through a low-cost and green hydrothermal method, without post-annealing or purification steps. We studied integrally the correlation among the structural, optical, textural, and electrical properties of the metal sulfides and their photocatalytic activity for hydrogen evolution and the degradation of indigo carmine dye.

FeS_2 exhibited the highest activities for hydrogen evolution (32 µmol g^{-1} h^{-1}) and indigo carmine degradation (88%), followed by CuS and NiS_2. The high activity of FeS_2
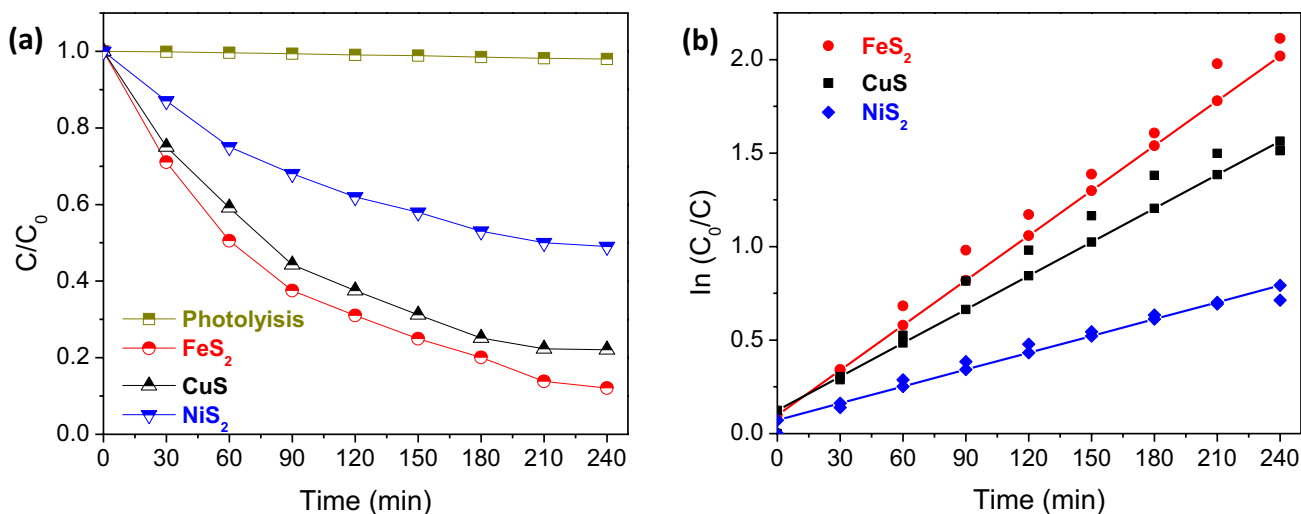
Fig. 15 **a** Photocatalytic degradation of indigo carmine over FeS_2, CuS and NiS_2 and **b** $\ln(C_0/C)$ as a function of the irradiation time

Table 5 Summary of the photocatalytic activity for indigo carmine degradation over the metal sulfides FeS_2, CuS, and NiS_2

Material	% Degradation of indigo carmine	Rate constant $k \times 10^{-3}$ (min^{-1})
FeS_2	88	8
CuS	78	6
NiS_2	51	3

was attributed to a higher crystallite size, smaller particle size and lower recombination, which promoted an enhanced charge separation, transport, and utilization. Additionally, three different sacrificial reagents (Na_2S/Na_2SO_3, EDTA, and ethanol) were studied for the hydrogen evolution reaction over the metal sulfides.

From the analysis of the energy band diagram we proposed that the lower oxidation potential of Na_2S/Na_2SO_3 improved the kinetics and yield of the reaction of hydrogen evolution in a higher proportion (15 times) than the other sacrificial reagents.
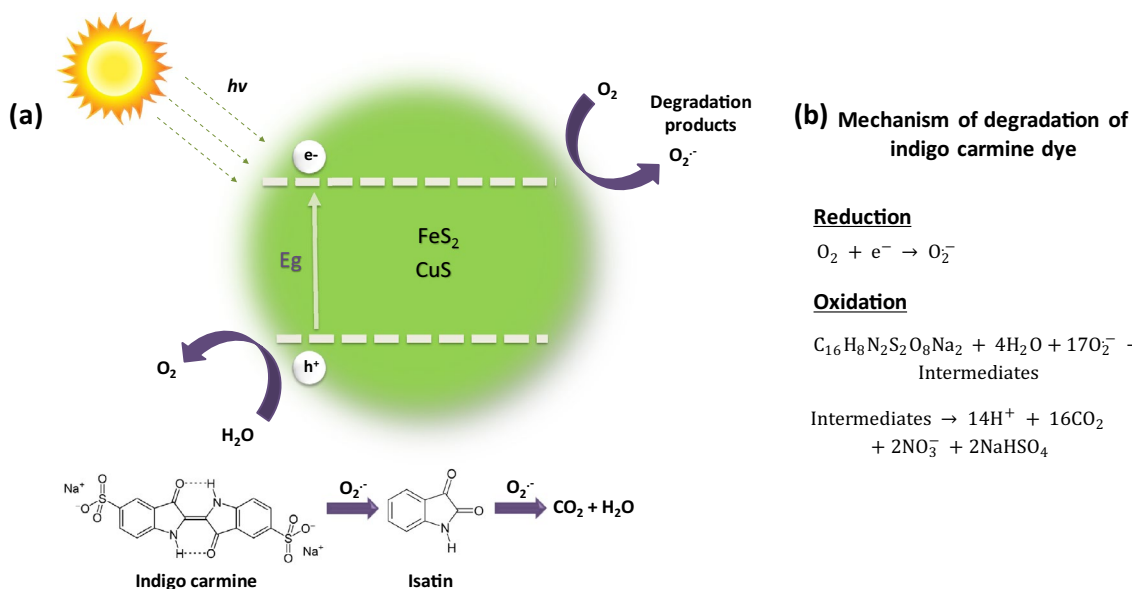

Fig. 16 **a** Photoexcitation and **b** mechanism of the photocatalytic degradation of indigo carmine dye over FeS_2 and CuS under simulated solar irradiation

The results presented here demonstrated the effect of three different sacrificial agents (an inorganic salt, an organic acid, and an alcohol) on the photocatalytic activity of the metal sulfides, according to the oxidation potential of the compounds. This approach can be applied along with other strategies (for example, the modification of the morphology, doping, formation of heterostructures, etc.) to further improve the efficiency of the hydrogen evolution reaction over these materials.

Moreover, the use of the sacrificial agents studied in this work can be extended not only to other sulfides and chalcogenides, but to semiconductors of different nature, including oxides, nitrides, etc. The complete characterization performed on the materials highlights their potential application not just in photocatalytic processes, but also for photovoltaic, electrochemical and optoelectronic devices.

The results obtained in this work indicated that FeS_2, CuS and NiS_2 are efficient alternative photocatalysts that can be employed in technological systems for hydrogen evolution from water splitting and the treatment of effluents containing indigo carmine and other similar dyes.

References

1. P. Wang, S. Sun, X. Zhang, X. Ge, W. Lu, Efficient degradation of organic pollutants and hydrogen evolution by g-C_3N_4 using melamine as the precursor and urea as the modifier. RSC Adv. **6**, 33589–33598 (2016)
2. J. Tian, Y. Leng, H. Cui, H. Liu, Hydrogenated TiO_2 nanobelts as highly efficient photocatalytic organic dye degradation and hydrogen evolution photocatalyst. J. Hazard. Mater. **299**, 165–173 (2015)
3. C.H. Lai, M.Y. Lu, L.J. Chen, Metal sulfides nanostructures: synthesis, properties and applications in energy conversion and storage. J. Mater. Chem. **22**, 19–30 (2012)
4. G. Kaur, B. Singh, P. Singh, K. Singh, A. Thakur, M. Kumar, R. Bala, A. Kumar, Iron disulfide (FeS_2): a promising material for removal of industrial pollutants. ChemistrySelect **2**, 2166–2173 (2017)
5. U. Shamraiz, R.A. Hussain, A. Badshah, Fabrication and applications of copper sulfide (CuS) nanostructures. J. Solid State Chem. **238**, 25–40 (2016)
6. P. Luo, H. Zhang, L. Liu, Y. Zhang, J. Deng, C. Xu, N. Hu, Y. Wang, Targeted synthesis of unique nickel sulfide (NiS, NiS_2) microarchitectures and the applications for the enhanced water splitting system. ACS Appl. Mater. Interfaces **9**, 2500–2508 (2017)
7. S. Liu, M. Li, S. Li, H. Li, L. Yan, Synthesis and adsorption/photocatalysis performance of pyrite FeS_2. Appl. Surf. Sci. **268**, 213–217 (2013)
8. S.K. Bhar, S. Jana, A. Mondal, N. Mukherjee, Photocatalytic degradation of organic dye on porous iron sulfide film surface. J. Colloid Interface Sci. **393**, 286–290 (2013)
9. S. Kansal, N. Kaur, S. Sing, Photocatalytic degradation of two commercial reactive dyes in aqueous phase using nanophotocatalysts. Nanoscale Res. Lett. **4**, 709–716 (2009)
10. A. Tian, Q. Xu, X. Shi, H. Yang, X. Xue, J. You, X. Wang, C. Dong, X. Yan, H. Zhou, Pyrite nanotube array films as an efficient photocatalyst for degradation of methylene blue and phenol. RSC Adv. **5**, 62724–62731 (2015)
11. X. Deng, C. Wang, H. Yang, M. Shao, S. Zhang, X. Wang, D. Meng, J. Huang, X. Xu, One-pot hydrothermal synthesis of CdS decorated CuS microflower-like structures for enhanced photocatalytic properties. Sci. Rep. **7**, 3877 (2017)
12. V.K. Gupta, D. Pathania, S. Agarwal, P. Singh, Adsorptional photocatalytic degradation of methylene blue onto pectin-CuS nanocomposite under solar light. J. Hazard. Mater. **243**, 179–186 (2012)
13. M. Tanveer, C. Cao, I. Aslam, Z. Ali, F. Idress, M. Tahir, W.S. Khan, F.K. Butt, A. Mahmood, Effect of the morphology of CuS upon the photocatalytic degradation of organic dyes. RSC Adv. **4**, 63447–63456 (2014)
14. D. Ayodhya, M. Venkatesham, A.S. Kumari, B. Reddy, D. Ramakrishna, G. Veerabhadram, Photocatalytic degradation of dye pollutants under solar, visible and UV light using green synthesized CuS nanoparticles. J. Exp. Nanosci. **11**, 418–432 (2016)
15. A. Molla, M. Sahu, S. Hussain, Synthesis of tunable band gap semiconductor nickel sulphide nanoparticles: rapid and round the clock degradation of organic dyes. Sci. Rep. **6**, 26034 (2016)
16. F. Soofivand, E. Esmaeili, M. Sabet, M. Salavati-Niasari, Simple synthesis, characterization and investigation of photocatalytic activity of NiS_2 nanoparticles using new precursors by hydrothermal method. J. Mater. Sci. Mater. Electron. **29**, 858–865 (2018)
17. S. Ammar, R. Abdelhedi, C. Flox, C. Arias, E. Brillas, Electrochemical degradation of the dye indigo carmine at boron-doped diamond anode for wastewaters remediation. Environ. Chem. Lett. **4**, 229–233 (2006)
18. R.E. Palma-Goyes, J. Silva-Agredo, I. González, R.A. Torres-Palma, Comparative degradation of indigo carmine by electrochemical oxidation and advanced oxidation processes. Electrochim. Acta **140**, 140:427–433 (2014)
19. M.A. Rauf, S. Salman-Ashraf, Fundamental principles and application of heterogeneous photocatalytic degradation of dyes in solution. Chem. Eng. J. **151**, 10–18 (2009)
20. M.R. Hoffmann, S.T. Martin, W.Y. Choi, D.W. Bahnemann, Environmental applications of semiconductor photocatalysis. Chem. Rev. **95**, 69–96 (1995)
21. L. Mi, Q. Ding, W. Chen, L. Zhao, H. Hoou, C. Liu, C. Shen, Z. Zheng, 3D porous nano/micro nickel sulfides with hierarchical structure: controlled synthesis, structure characterization and electrochemical properties. Dalton Trans. **42**, 5724–5730 (2013)
22. T. Zhu, H.B. Wu, Y. Wang, R. Xu, X.W.D. Lou, Formation of 1D hierarchical structures composed of Ni_3S_2 nanosheets on CNTs backbone for supercapacitors and photocatalytic H_2 production. Adv. Energy Mater. **2**, 1497–1502 (2012)
23. W.S. Chi, J.W. Han, S. Yang, D.K. Roh, H. Lee, J.H. Kim, Employing electrostatic self-assembly of tailored nickel sulfide nanoparticles for quasi-solid-state dye-sensitized solar cells with Pt-free counter electrodes. Chem. Commun. **48**, 9501–9503 (2012)
24. F. Ghribi, A. Alyamani, A.B. Ayadi, K. Djessas, L.E. Mir, Study of CuS thin films for solar cell applications sputtered from nanoparticles synthesised by hydrothermal route. Energy Procedia **84**, 197–203 (2015)

25. M. Cabán-Acevedo, M.S. Faber, Y. Tan, R.J. Hamers, S. Jin, Synthesis and properties of semiconducting iron pyrite (FeS_2) nanowires. Nano Lett. **12**, 1977–1982 (2012)

26. S. Khalid, E. Ahmed, M.A. Malik, D.J. Lewis, S.A. Bakar, Y. Khan, P. O'Brien, Synthesis of pyrite thin films and transition metal doped pyrite thin films by aerosol-assisted chemical vapour deposition. New J. Chem. **39**, 1013–1021 (2015)

27. M.S. Faber, M.A. Lokowski, Q. Ding, N.S. Kaiser, S. Jin, Earth-abundant metal pyrites (FeS_2, CoS_2, NiS_2, and their alloys) for highly efficient hydrogen evolution and polysulfide reduction electrocatalysis. J. Phys. Chem. C **118**, 21347–21356 (2014)

28. H. Ren, W. Xu, S. Zhu, Z. Cui, X. Yang, A. Inoue, Synthesis and properties of nanoporous Ag_2S/CuS catalyst for hydrogen evolution reaction. Electrochim. Acta **190**, 221–228 (2016)

29. T. An, Y. Wang, J. Tang, W. Wei, X. Cui, A.M. Alenizi, L. Zhang, G. Zheng, Interlaced NiS_2-MoS_2 nanoflake-nanowires as efficient hydrogen evolution electrocatalysts in basic solutions. J. Mater. Chem. A **4**, 13439–13443 (2016)

30. Q. Wang, G. Yun, Y. Bai, N. An, Y. Chen, R. Wang, Z. Lei, W. Shangguan, CuS, NiS as co-catalyst for enhanced photocatalytic hydrogen evolution over TiO_2. Int. J. Hydrog. Energy **39**, 13421–13428 (2014)

31. L. Xiao, H. Chen, J. Huang, Visible light-driven photocatalytic H_2-generation activity of CuS/ZnS composite particles. Mater. Res. Bull. **64**, 370–374 (2015)

32. A. Galińska, J. Walendziewski, Photocatalytic water splitting over Pt-TiO_2 in the presence of sacrificial reagents. Energy Fuels **19**, 1143–1147 (2005)

33. K. Chan, C. Tsai, H.A. Hansen, J.K. Nørskov, Molybdenum sulfides and selenides as possible electrocatalysts for CO_2 reduction. ChemCatChem **6**(7), 1899–1905 (2014)

34. T. Shinagawa, G.O. Larrazábal, A.J. Martín, F. Krumeich, J. Pérez-Ramírez, Sulfur-modified copper catalysts for the electrochemical reduction of carbon dioxide to formate. ACS Catal. **8**, 837–844 (2018)

35. S. Zhao, S. Guo, C. Zhu, J. Gao, H. Li, H. Huang, Y. Liu, Z. Kang, Achieving electroreduction of CO_2 to CH_3OH with high selectivity using a pyrite-nickel sulfide nanocomposite. RSC Adv. **7**, 1376–1381 (2017)

36. A. Roldan, N. Hollingsworth, A. Roffey, H.U. Islam, J.B.M. Goodall, C.R.A. Catlow, J.A. Darr, W. Bras, G. Sankar, K.B. Holt, G. Hogarth, N.H. de Leeuw, Bio-inspired CO_2 conversion by iron sulfide catalysts under sustainable conditions. Chem. Commun. **51**, 7501–7504 (2015)

37. F. Li, J.F. Wu, Q.H. Qin, Z. Li, X.T. Huang, Controllable synthesis, optical and photocatalytic properties of CuS nanomaterials with hierarchical structures. Powder Technol. **198**, 267–274 (2010)

38. H. Wang, H.R. Zhang, X.N. Zhao, S. Xu, J.J. Zhu, Preparation of copper monosulfide and nickel monosulfide nanoparticles by sonochemical method. Mater. Lett. **55**, 253–258 (2002)

39. C. Nascu, I. Pop, V. Ionescu, E. Indrea, I. Bratu, Spray pyrolysis deposition of CuS thin films. Mater. Lett. **32**, 73–77 (1997)

40. J.P. Da Costa, A.V. Girão, J.P. Lourenço, O.C. Monteiro, T. Trindade, Green synthesis of covellite nanocrystals using biologically generated sulfide: potential for bioremediation systems. J. Environ. Manag. **128**, 226–232 (2013)

41. L. Sze-Mun, S. Jin-Chung, A. Ahmad-Zuhairi, M. Abdul-Rahman, Green hydrothermal synthesis of ZnO nanotubes for photocatalytic degradation of methylparaben. Mater. Lett. **93**, 423–426 (2013)

42. P. Anastas, N. Eghbali, Green chemistry: principles and practice. Chem. Soc. Rev. **39**, 301–312 (2010)

43. R.A. Spurr, H. Myers, Quantitative analysis of anatase-rutile mixtures with an X-ray diffractometer. Anal. Chem. **29**, 760–762 (1957)

44. T. Sreethawong, Y. Suzuki, S. Yoshikawa, Synthesis, characterization and photocatalytic activity for hydrogen evolution of nanocrystal-line mesoporous titania prepared by surfactant-assisted templating sol-gel process. J. Solid State Chem. **178**, 329–338 (2005)

45. B. Wickman, A.B. Fanta, A. Burrows, A. Hellman, J.B. Wagner, B. Iandolo, Iron oxide films prepared by rapid thermal processing for solar energy conversion. Sci. Rep. **7**, 40500 (2017)

46. S. Kumar, R. Parthasarathy, A.P. Singh, B. Wickman, M. Thirumal, A.K. Ganguli, Dominant {100} facet selectivity for enhanced photocatalytic activity of $NaNbO_3$ in $NaNbO_3$/CdS core/shell heterostructures. Catal. Sci. Technol. **7**, 481–495 (2017)

47. I. Vamvasakis, B. Liu, G.S. Armatas, Size effects of platinum nanoparticles in photocatalytic hydrogen production over 3D mesoporous networks of CdS and Pt nanojunctions. Adv. Funct. Mater. **26**, 8062–8071 (2016)

48. A.M. Huerta-Flores, L.M. Torres-Martínez, D. Sánchez-Martínez, M.E. Zarazúa-Morín, $SrZrO_3$ powders: alternative synthesis, characterization and application as photocatalysts for hydrogen evolution from water splitting. Fuel **158**, 66–71 (2015)

49. Y. Bi, Y. Yuan, C.L. Exstrom, S.A. Darveau, J. Huang, Air stable, photosensitive, phase pure iron pyrite nanocrystal thin films for photovoltaic application. Nano Lett. **11**, 4953–4957 (2011)

50. W. Xu, S. Zhu, Y. Liang, Z. Li, Z. Cui, X. Yang, A. Inoue, Nanoporous CuS with excellent photocatalytic property. Sci. Rep. **5**, 18125 (2015)

51. N. Jiang, Q. Tang, M. Sheng, B. You, D. Jiang, Y. Sun, Nickel sulphides for electrocatalytic hydrogen evolution under alkaline conditions: a case study of crystalline NiS, NiS_2, and Ni_3S_2 nanoparticles. Catal. Sci. Technol. **6**, 1077–1084 (2016)

52. H. Wang, S. Li, Y. Liu, J. Ding, Y.H. Lin, H. Xu, B. Xu, C.W. Nan, $Bi_{1−x}La_xCuSeO$ as new tunable full solar light active photocatalysts. Sci. Rep. **6**, 24620 (2016)

53. J. Rouquerol, D. Avnir, C.W. Fairbridge, D.H. Everett, J.M. Haynes, N. Pernicone, J.D.F. Ramsay, K.S.W. Sing, K.K. Unger. Recommendations for the characterization of porous solids (technical report). Pure Appl. Chem. **66**(8), 1739–1758 (1994)

54. K.S.W. Sing, Reporting physisorption data for gas/solid systems with special reference to the determination of surface area and porosity (recommendations 1984). Pure Appl. Chem. **57**(4), 603–619 (1985)

55. J.C. Yu, A. Xu, L. Zhang, R. Song, L. Wu, Synthesis and characterization of porous magnesium hydroxide and oxide nanoplates. J. Phys. Chem. B **108**, 64–70 (2004)

56. A.T.T. Do, H.T. Giang, T.T. Do, N.Q. Pham, G.T. Ho, Effect of palladium on the optical and hydrogen sensing characteristics of Pd-doped ZnO nanoparticles. Bellstein J. Nanotechnol. **5**, 1261–1267 (2014)

57. K. Sing, The use of nitrogen adsorption for the characterisation of porous materials. Colloids Surf. A **187–188**, 3–9 (2001)

58. S. Khalid, M.A. Malik, D.J. Lewis, P. Kevin, E. Ahmed, Y. Khan, P. O'Brien, Transition metal doped pyrite (FeS_2) thin films: structural properties and evaluation of optical and band energies. J. Mater. Chem. C **3**, 12068–12076 (2017)

59. H. Man, C. Wang, Y. Sun, Y. Ning, P. Song, W. Huang, Studies on Cs_xWO_3/BiOCl composite as a novel visible light droven photocatalyst. J. Materiomics **2**, 338–343 (2016)

60. X. Gao, X. Liu, Z. Zhu, X. Wang, Z. Xie, Enhanced photoelectrochemical and photocatalytic behaviors of MFe_2O_4 (M = Ni, Co, Zn and Sr) modified TiO_2 nanorod arrays. Sci. Rep. **6**, 30543 (2016)

61. P. Kumar, P. Sharma, R. Shrivastav, S. Dass, V.R. Satsangi, Electrodeposited zirconium-doped a-Fe_2O_3 thin film for photoelectrochemical water splitting. Int. J. Hydrog. Energy **36**, 2777–2784 (2011)

62. I. Cesar, K. Sivula, A. Kay, R. Zboril, M. Grätzel, Influence of feature size, film thickness, and silicon doping on the performance

of nanostructured hematite photoanodes for solar water splitting. J. Phys. Chem. C **113**(2), 772–782 (2009)

63. P.C.K. Vesborg, B. Seger, I. Chorkendorff, Recent development in hydrogen evolution reaction catalysts and their practical implementation. J. Phys. Chem. Lett. **6**, 951–957 (2015)

64. X. Zou, Y. Zhang, Noble metal-free hydrogen evolution catalysts for water splitting. Chem. Soc. Rev. **44**, 5148–5180 (2015)

65. Y. Zheng, Y. Jiao, M. Jaroniec, S.Z. Qiao, Advancing the electrochemistry of the hydrogen-evolution reaction through combining experiment and theory. Angew. Chem. Int. Ed. **54**, 52–65 (2015)

66. M. Wang, S. Shen, L. Li, Z. Tang, J. Yang, Effects of sacrificial reagents on photocatalytic hydrogen evolution over different photocatalysts. J. Mater. Sci. **52**, 5155–5164 (2017)

67. D.S. Muggli, J.T. McCue, J.L. Falconer, Mechanism of the photocatalytic oxidation of ethanol on TiO_2. J. Catal. **173**(2), 470–483 (1998)

68. Q. Wang, J. Li, Y. Bai, J. Lian, H. Huang, Z. Li, Z. Lei, W. Shangguan, Photochemical preparation of Cd/CdS photocatalysts and their efficient photocatalytic hydrogen production under visible light irradiation. Green Chem. **16**, 2728–2735 (2014)

69. H. Ji, Y. Fan, J. Yan, Y. Xu, X. She, J. Gu, T. Fei, H. Xu, H. Li, Construction of SnO_2/graphene-like g-C_2N_4 with enhanced visible light photocatalytic activity. RSC Adv. **7**, 36101–36111 (2017)

70. J. Carretero-González, E. Castillo-Martínez, M. Armand, Highly water-soluble three-redox state organic dyes as bifunctional analytes. Energy Environ. Sci. **9**, 3521–3530 (2016)